Facile Synthesis toward the Optimal Structure-Conductivity Characteristics of the Argyrodite Li6PS5Cl Solid-State Electrolyte

Yu, Chuang; Ganapathy, Swapna; Hageman, Jart; Van Eijck, Lambert; Van Eck, Ernst R.H.; Zhang, Long; Schwietert, Tammo; Basak, Shibabrata; Kelder, Erik M.; Wagemaker, Marnix

DOI
10.1021/acsami.8b07476

Publication date
2018

Document Version
Final published version

Published in
ACS Applied Materials and Interfaces

ACS APPLIED MATERIALS & INTERFACES

Research Article

Cite This: ACS Appl. Mater. Interfaces 2018, 10, 33296−33306

www.acsami.org

Facile Synthesis toward the Optimal Structure-Conductivity Characteristics of the Argyrodite Li_6PS_5Cl Solid-State Electrolyte

Chuang Yu,[†] Swapna Ganapathy,[†] Jart Hageman,[†] Lambert van Eijck,[†] Ernst R. H. van Eck,[‡] Long Zhang,[§] Tammo Schwietert,[†] Shibabrata Basak,[†] Erik M. Kelder,[†] and Marnix Wagemaker*[,†]

[†]Department of Radiation Science and Technology, Delft University of Technology, Mekelweg 15, 2629 JB Delft, The Netherlands
[‡]Institute for Molecules and Materials, Radboud University Nijmegen, Heyendaalseweg 135, 6525 AJ Nijmegen, The Netherlands
[§]State Key Laboratory of Metastable, Materials Science and Technology, Yanshan University, 066004 Qinhuangdao, Hebei, China

Supporting Information

ABSTRACT: The high Li-ion conductivity of the argyrodite Li_6PS_5Cl makes it a promising solid electrolyte candidate for all-solid-state Li-ion batteries. For future application, it is essential to identify facile synthesis procedures and to relate the synthesis conditions to the solid electrolyte material performance. Here, a simple optimized synthesis route is investigated that avoids intensive ball milling by direct annealing of the mixed precursors at 550 °C for 10 h, resulting in argyrodite Li_6PS_5Cl with a high Li-ion conductivity of up to 4.96×10^{-3} S cm^{-1} at 26.2 °C. Both the temperature-dependent alternating current impedance conductivities and solid-state NMR spin−lattice relaxation rates demonstrate that the Li_6PS_5Cl prepared under these conditions results in a higher conductivity and Li-ion mobility compared to materials prepared by the traditional mechanical milling route. The origin of the improved conductivity appears to be a combination of the optimal local Cl structure and its homogeneous distribution in the material. All-solid-state cells consisting of an $80Li_2S−20LiI$ cathode, the optimized Li_6PS_5Cl electrolyte, and an In anode showed a relatively good electrochemical performance with an initial discharge capacity of 662.6 mAh g^{-1} when a current density of 0.13 mA cm^{-2} was used, corresponding to a C-rate of approximately C/20. On direct comparison with a solid-state battery using a solid electrolyte prepared by the mechanical milling route, the battery made with the new material exhibits a higher initial discharge capacity and Coulombic efficiency at a higher current density with better cycling stability. Nevertheless, the cycling stability is limited by the electrolyte stability, which is a major concern for these types of solid-state batteries.

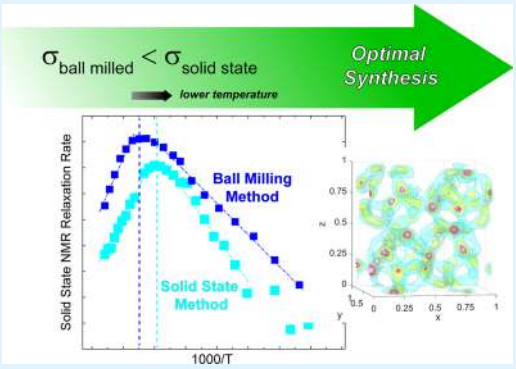

KEYWORDS: *sulfide solid electrolyte, argyrodite, structure, conductivity, solid-state batteries*

INTRODUCTION

The advent of the highly conductive sulfide-based solid electrolytes has put all-solid-state batteries back into the spotlight.[1−7] These materials possess room temperature conductivities comparable to that of liquid electrolytes making them prime candidates for use in all-solid-state batteries. Such battery systems are attractive due to the inherently higher battery safety they provide.[8−10] An important family of the sulfide-based solid electrolytes is the Li-argyrodite Li_6PS_5X (X = Cl, Br, and I) providing Li-ion conductivities of up to 10^{-3} S cm^{-1} at room temperature.[11,12] The high conductivity and the low-cost of the starting materials make the Li-argyrodite a viable candidate for application in all-solid-state batteries.

Currently, the most commonly used method to prepare Li-argyrodites is high-energy mechanical milling for long durations (Li_2S, P_2S_5, and LiCl/Br/I at >500 rpm for >10 h) followed by annealing (550 °C for Li_6PS_5Cl and 300 °C for Li_6PS_5Br).[13,14] However, this route is less efficient being time and energy intensive due to the high rotation speeds and long milling durations required. Additionally, with this synthesis route, it is difficult to obtain homogenous materials reproducibly because of the high-speed milling process involved.[15] An alternative wet chemical synthesis route based on a dissolution−precipitation process via ethanol solution was successfully proposed by Yubuchi et al.,[16] resulting in a homogenous Li_6PS_5Cl electrolyte. However, the ionic conductivity of the Li_6PS_5Cl electrolyte prepared with this route was 10^{-4} S cm^{-1} at room temperature, significantly lower than that synthesized by the milling method.[16,17] Deiseroth et al. and more recently Kraft et al. both used direct heating of the precursor mixtures to obtain the lithium argyrodites Li_6PS_5X (X = Cl, Br, and I),[11,18] which is a more time and energy conserving route, also suitable for larger-scale synthesis of these materials. The synthesis route may influence the detailed

Received: May 7, 2018
Accepted: September 10, 2018
Published: September 10, 2018

structural properties that are responsible for the Li-ion conductivity. The highest room temperature Li-ion conductivities reported for Li_6PS_5Cl and Li_6PS_5Br have values up to 10^{-3} S cm^{-1}.[12,13] It has been shown that the halogen distribution over the sulfur sub-lattice has a critical influence on the Li-ion conductivity.[12] Molecular dynamics (MD) simulations have suggested that the distribution of the halogen over 4a and 4c sulfur sites determines the jump frequency of all three kinds of Li-ion jumps in the Li-argyrodite, i.e., doublet, intra-cage, and inter-cage, maximizing the slowest jump frequency at 75% occupancy of the halogen on the 4c sites. Furthermore, it has been suggested that a homogeneous distribution of the halogen in the material is important, as this homogeneously distributes halogen charge compensating vacancies through the lattice.[19] Kraft et al.[18] have demonstrated that the softness of the lattice, a consequence of the polarizability of the halogen atoms, simultaneously leads to a lower activation energy,[20] and lower attempt frequency for diffusion, such that there typically exists an optimal balance to achieve the highest Li-ion conductivity. Therefore, developing and optimizing synthesis conditions should go hand in hand with detailed structural considerations, so as to achieve materials with optimal Li-ion conductivity.

Here, the argyrodite Li_6PS_5Cl, prepared using direct synthesis[11,18] is investigated in detail and compared with Li_6PS_5Cl prepared using the conventional mechanical milling method.[15,21] The present solid-state method (referred to as the SSM route) entails the simple mixing of the precursors followed by annealing. The annealing temperature was varied to achieve optimal synthesis conditions, resulting in higher Li-ion conductivities for Li_6PS_5Cl compared to that of the material prepared by the conventional mechanical milling route followed by annealing (ball milling annealing (BMA) route). A detailed correlation between the structure and conductivity is established via X-ray diffraction (XRD), neutron diffraction (ND), temperature-dependent alternating current (AC) impedance spectroscopy, and ^{7}Li spin−lattice relaxation (SLR) NMR. Finally, all-solid-state batteries using the optimized Li_6PS_5Cl solid electrolyte in combination with an $80Li_2S$−20LiI cathode were assembled and characterized.

METHODS

Reagent-grade Li_2S (99.98%, Sigma-Aldrich), P_2S_5 (99%, Sigma-Aldrich), and LiCl (99.0%, Sigma-Aldrich) crystalline powders were used as starting materials. The required amounts of starting materials were sealed in a tungsten carbide (WC)-coated (inner) stainless-steel jar with 10 WC balls (8 g/ball) in an argon-filled glovebox (H_2O, O_2 < 0.3 ppm) because of the reactivity of the sample with oxygen and moisture. The total weight of the starting mixture was approximately 3.0 g. The mixture was first ball-milled with a speed of 110 rpm for 1 h to ensure the homogeneity of the obtained raw mixture, after which it was sealed in a quartz tube and annealed at various temperatures (300, 350, 400, 500, 550, and 600 °C) for 10 h to investigate the optimum synthesis temperature to achieve phase-pure Li_6PS_5Cl with high lithium ion conductivity. The sample obtained from the above route will be referred to as SSM-Li_6PS_5Cl. While the sample prepared by the mechanical milling process was named as BM-Li_6PS_5Cl and the sample obtained from the mechanical milling followed by a heat treatment route was named as BMA-Li_6PS_5Cl, where more details on the ball-milled route materials can be found in previous work.[15,21]

Powder XRD patterns were collected over a 2θ range of 10−100° to identify the crystalline phases of different materials using Cu Kα X-rays (λ = 1.5406 Å at 45 kV and 40 mA) on an X'Pert Pro X-ray diffractometer (PANalytical). To prevent the reaction with moisture and oxygen, the powders were sealed in an air-tight XRD sample holder in an argon-filled glovebox. Neutron diffraction data were collected on the new neutron powder diffractometer PEARL of the TU Delft. The data were collected at room temperature using the (533) reflection of the germanium monochromator (λ = 1.665 Å). The sample was loaded under argon in a 6 mm diameter air-tight vanadium sample can. The sample was measured for 18 h from 10.4 to 160° 2θ. The data treatment consisted of a detection efficiency correction for each of the 1408 detector pixels and a subtraction of the background, caused by the instrument and the sample can. The X-ray and neutron diffraction data were refined simultaneously using the Rietveld method implemented in General Structure Analysis System (GSAS).[22,23] The morphological characterization of the material was performed with a scanning electron microscope (SEM, Hitachi S-4800 II FESEM). For the transmission electron microscopy (TEM) measurements, a suspension of Li_6PS_5Cl in hexane was prepared which was dropcast onto a standard gold TEM grid with a holey carbon film, inside an argon-filled glovebox. To prevent the contact with air or moisture, the TEM grid with the sample was loaded into a custom-made vacuum transfer TEM holder. TEM measurements were performed on an FEI-Tecnai operating at 200 kV.

The ionic conductivity of the Li_6PS_5Cl electrolyte material was determined by AC impedance spectroscopy. Samples for the measurement were prepared by pressing 300 mg of Li_6PS_5Cl powder into a pellet with a 10 mm diameter under a pressure of 8 tons for 1 min. Stainless-steel disks were attached to both faces of the pellet. AC impedance measurements were performed using an Autolab (PGSTAT302N) in the frequency range of 1 Hz to 1 MHz with an applied voltage of 0.01 V.

Solid-state NMR measurements were performed on a Chemagnetics 400 Infinity spectrometer (B_0 = 9.4 T), operating at a ^{7}Li resonance frequency of 155.506 MHz. The $\pi/2$ pulse length was determined to be 3.1 μs with an radio frequency field strength of 75 kHz. Chemical shifts were referenced with respect to a 0.1 M LiCl solution. The air sensitive Li_6PS_5Cl samples were sealed in custom-made Teflon tubes in an argon-filled glovebox (H_2O, O_2 < 0.3 ppm). Variable temperature measurements were performed using a 5 mm static goniometer probe. Spectra were acquired in the temperature range of −100 to +180 °C. T_1 relaxation times were determined at various temperatures using a saturation recovery experiment.

Laboratory-scale solid-state Li_2S/SSM-Li_6PS_5Cl/In and $80Li_2S$−20LiI/SSM-Li_6PS_5Cl/In batteries were prepared. For the Li_2S/SSM-Li_6PS_5Cl/In solid-state cell, the cathode mixture was prepared as follows: commercial Li_2S was milled with a rotation speed of 500 rpm for 4 h, and then subsequently mixed with SSM-Li_6PS_5Cl, super P (TIMCAL), and carbon nanofiber (CNF) with a weight ratio of 5:4:0.5:0.5 using a rotation speed of 510 rpm for 10 h to obtain the final cathode mixture. For the $80Li_2S$−20LiI/SSM-Li_6PS_5Cl/In solid-state cell, the cathode mixture was prepared as follows: commercial Li_2S was first mixed with LiI with the designated ratio (mol %) and milled with a rotation speed of 110 rpm for 1 h, and then subsequently milled with SSM-Li_6PS_5Cl, super P (TIMCAL), and carbon nanofiber (CNF) with a weight ratio of 5:4:0.5:0.5 using a rotation speed of 510 rpm for 10 h to obtain the final cathode mixture. A two-layer pellet, 10 mm in diameter, consisting of ∼7.64 to 9.55 mg cm^{-2} of the above-described cathode mixture and 140 mg of SSM-Li_6PS_5Cl solid electrolyte, was obtained by pressing the electrode and electrolyte powders together by applying 6 tons of pressure. A disc of In foil was subsequently attached to the other side. Finally, the full solid-state battery pellet was pressed with 2 tons of pressure for 30 s. The assembled cell was charged and discharged by applying a current density of 0.13 mA cm^{-2} between 0 and 3.0 V vs In to evaluate its electrochemical performance. The obtained capacity was normalized by the weight of Li_2S and Li_2S−LiI in the cathode, respectively.

To demonstrate the position of the Li-ions and the Li-ion diffusion pathways in Li_6PS_5Cl a density functional theory (DFT) MD simulation is performed similar to previous research.[19] The DFT MD simulations are performed using the Vienna ab initio simulation package (VASP) within the GGA approximation and utilizing the PAW-PBE basis set with a cutoff energy of 280 eV. The simulations use one unit cell with periodic boundary conditions. The structure is

DOI: 10.1021/acsami.8b07476
ACS Appl. Mater. Interfaces 2018, 10, 33296−33306

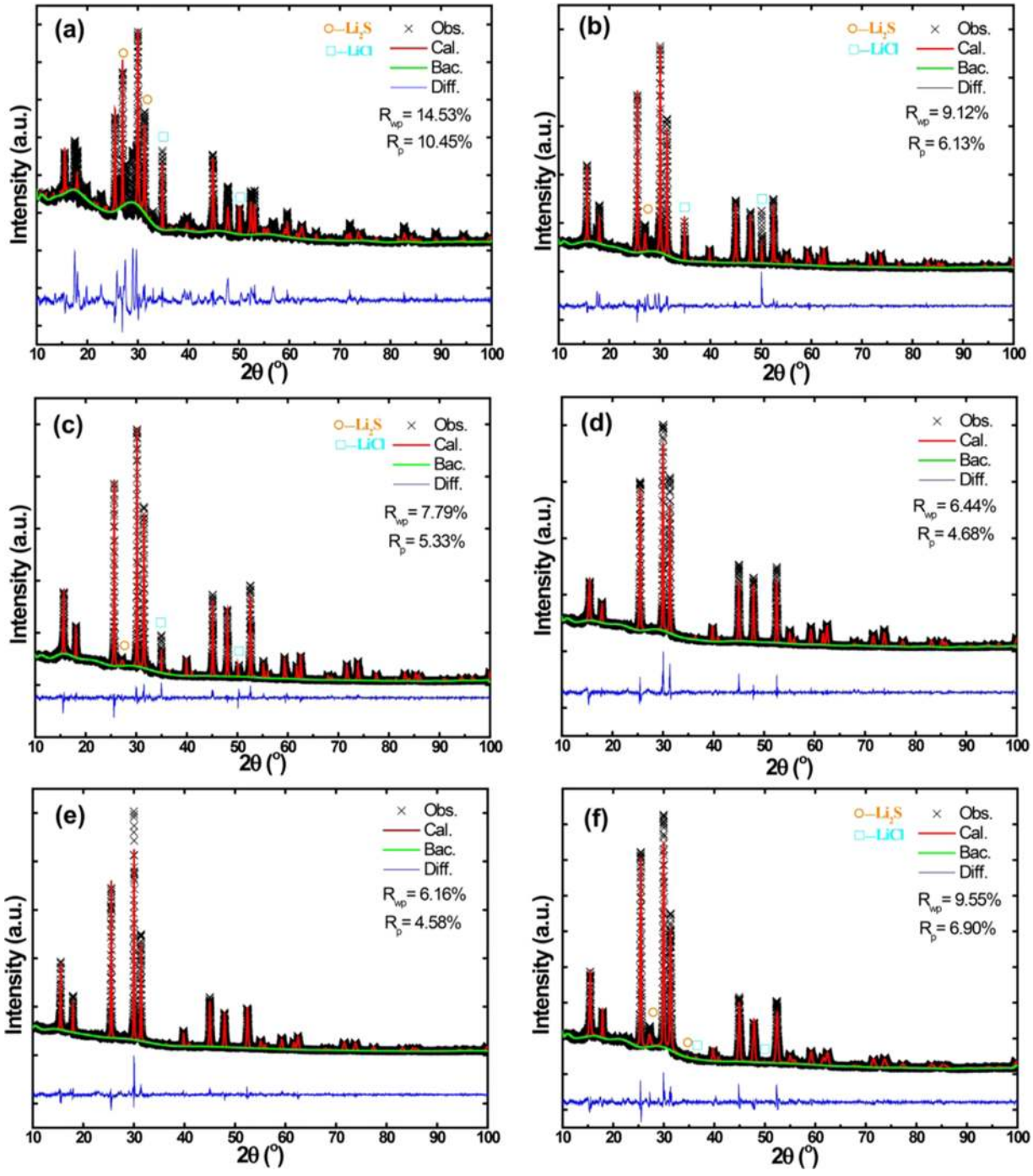

Figure 1. Rietveld refinement of XRD data for the pristine precursor mixture annealed at various temperatures: (a) 300 °C, (b) 350 °C, (c) 400 °C, (d) 500 °C, (e) 550 °C, and (f) 600 °C.

first relaxed with a 4 x 4 x 4 *k*-point mesh after which the number of *k*-points is reduced to 1 x 1 x 1. Simulations are performed in the NVT ensemble for 100 ps with 2 fs time steps, the temperature is scaled every 1000 time steps.

RESULTS AND DISCUSSION

To prepare a homogeneous mixture, the precursor materials (Li_2S, P_2S_5, and LiCl) were mixed and ball-milled at a low rotation speed of 110 rpm for 1 h. The obtained mixture was then sealed in several quartz tubes, each of which was annealed at a different temperature, from 300 to 600 °C for 10 h each to determine the optimum annealing temperature. The XRD patterns of the samples obtained after annealing are shown in Figure 1. For the sample annealed at 300 °C, the reflections originating from the Li_2S and LiCl precursors can still be observed. As the annealing temperature is increased, the reflections from Li_2S and LiCl decrease and from the cubic $F\bar{4}3m$ Li_6PS_5Cl phase increase. For annealing temperatures of 500 and 550 °C, the pure Li_6PS_5Cl phase is obtained, representing the cubic $F\bar{4}3m$ structure as shown in Figure 2a. However, for the sample prepared with an annealing temperature of 600 °C, the reflections associated with Li_2S and LiCl appear again. Rietveld refinement of the XRD patterns as implemented in GSAS,[23] was performed including

DOI: 10.1021/acsami.8b07476
ACS Appl. Mater. Interfaces 2018, 10, 33296−33306

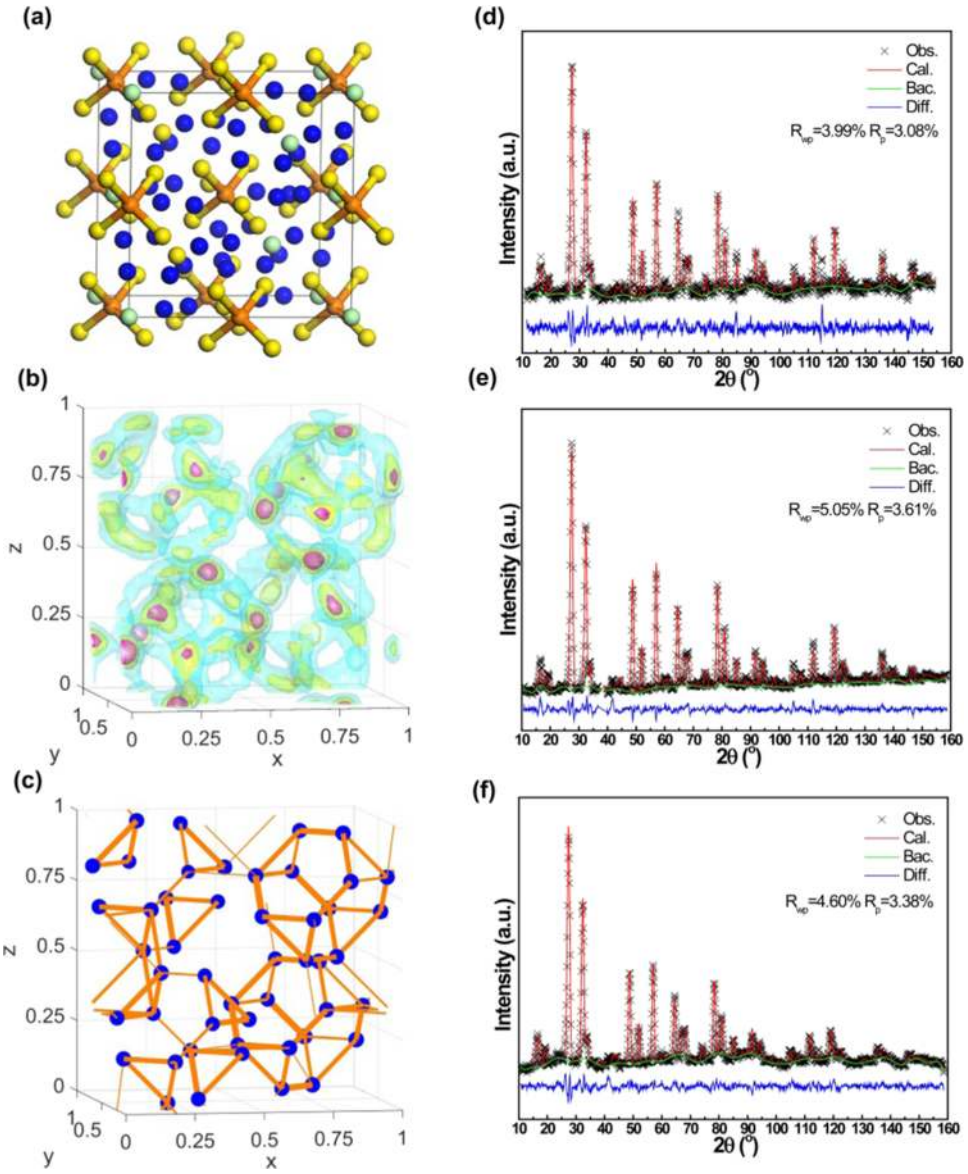

Figure 2. (a) Unit cell of argyrodite Li_6PS_5Cl in the $F\bar{4}3m$ space group. Blue spheres represent Li atoms, orange represents phosphorous, yellow represents sulfur, and green represents chloride atoms. (b) Li-ion density of Li_6PS_5Cl at 500 K during a DFT-based MD simulation demonstrates the diffusion pathway. The red surfaces correspond to higher Li-ion densities and blue surfaces to lower densities. The *x*, *y*, and *z* coordinates are given in fractional coordinates. (c) The jump statistic plot between different Li sites resulting from the DFT-based MD simulation shown in (b). The blue spheres indicate the 48h Li sites in the $F\bar{4}3m$ group. The orange lines indicate jumps between the lattice sites. Thicker lines indicate higher jump rates. Neutron diffraction patterns including their Rietveld refinement for the pristine SSM-Li_6PS_5Cl material prepared by annealing at various synthesis temperatures: (d) 500 °C, (e) 550 °C, and (f) 600 °C.

the precursor phases and the cubic Li_6PS_5Cl (space group $F\bar{4}3m$). To investigate the morphology and the distribution of sulfur for the Li_6PS_5Cl synthesized by the solid-state method, SEM and TEM were performed on the SSM-Li_6PS_5Cl annealed at 550 °C. The SEM and TEM images are shown in Figure S1. The energy-dispersive X-ray spectroscopy mapping result shows a homogenous distribution of S in the obtained SSM-Li_6PS_5Cl.

To demonstrate the lithium sites and diffusion pathways in Li_6PS_5Cl, density functional theory (DFT) molecular dynamics (MD) simulations were performed similar to previous research,[19] the results of which are shown in Figure 2b,c. The cage like diffusion connecting the 48h sites is clearly recognized where the inter-cage diffusion was previously reported to limit the macroscopic diffusion.[19] To gain detailed insight into the impact of the synthesis on the argyrodite structure, additional neutron diffraction (ND) was performed on the samples obtained after annealing at 500, 550, and 600 °C, respectively, which are shown in Figure 2d–f. The neutron diffraction patterns were simultaneously refined with the XRD patterns measured for the same samples (Figure 1d–f). ND is in particular important for determining the Li-ion positions and the Cl/S distribution over the 4a and 4c sites which has been shown to be a key parameter for the ionic conductivity.[12,18,21]

During the refinement, shown in Figures 1 and 2, the sum of the S and Cl occupancy on the 4a (0,0,0) and 4c (1/4,1/4,1/4) positions has been restricted to unity, whereas the occupancy of Li is not restricted. The mean square displacement (Uiso) of the atoms on the 4a and 4c positions

DOI: 10.1021/acsami.8b07476
ACS Appl. Mater. Interfaces 2018, 10, 33296–33306

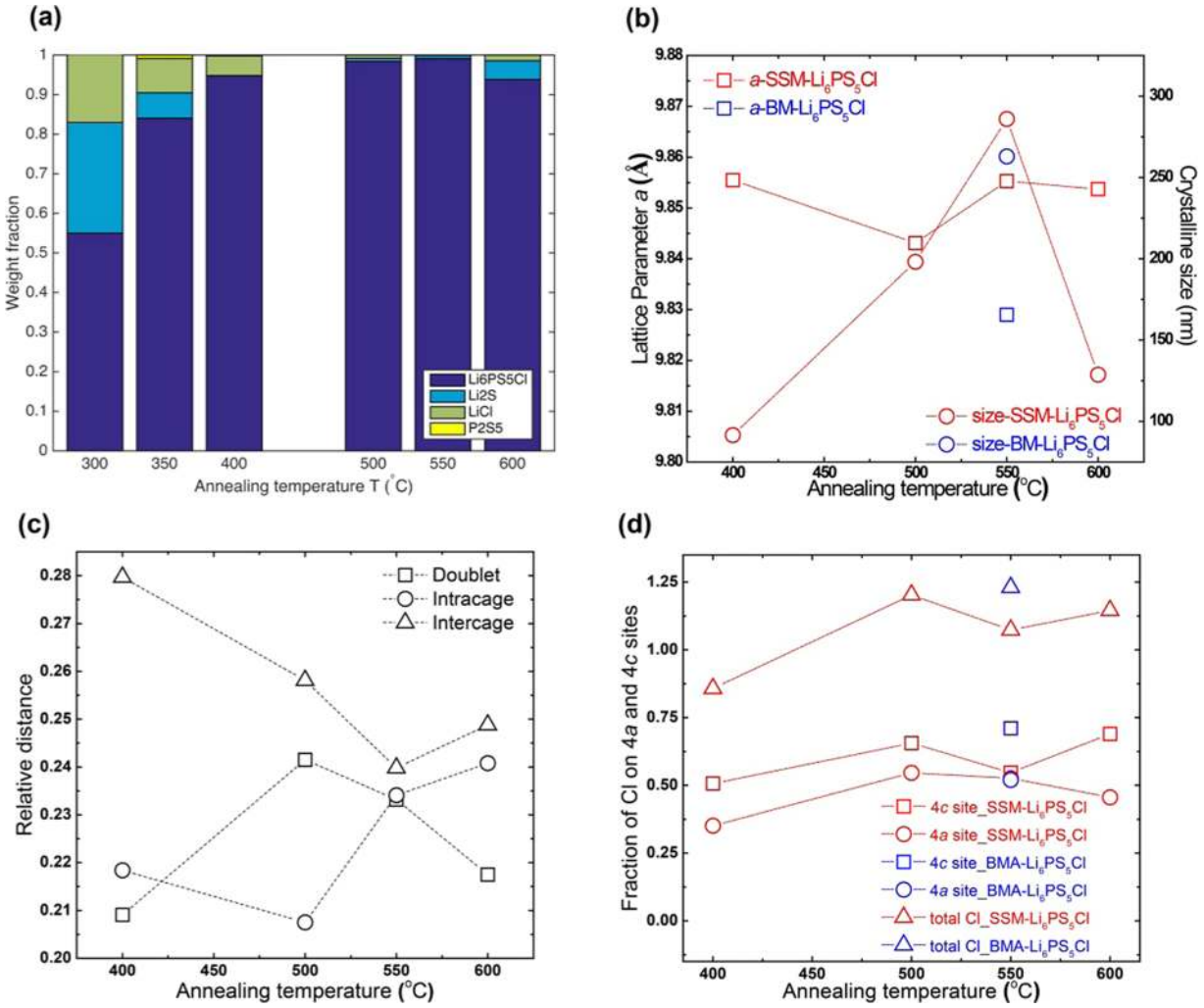

Figure 3. (a) Phase fractions from XRD refinement of SSM-Li_6PS_5Cl annealed at various temperatures (300, 350, 400, 500, 550, and 600 °C). (b) The crystallite size and lattice parameters, all resulting from simultaneous refinement of the XRD and ND patterns of SSM-Li_6PS_5Cl obtained after various annealing temperatures and of the conventionally prepared BMA-Li_6PS_5Cl material (by mechanical milling followed by annealing). (c) Inter-cage, intra-cage, and doublet relative jump distance of Li-ions of SSM-Li_6PS_5Cl annealed at various temperatures. (d) the distribution of Cl on the 4c and 4a sites and the total Cl composition.

were coupled during the refinement, and the atomic displacement factor of the lithium ions was set as anisotropic. The results of the Rietveld refinement of the Li_6PS_5Cl samples prepared by annealing (400−600 °C) as well as the material prepared by the conventional mechanical milling method are summarized in the Supporting Information Tables S1−S5. The resulting phase contributions after annealing at different temperatures are shown in Figure 3a, demonstrating that the purest phase of Li_6PS_5Cl can be obtained by annealing the precursor mixture at 500 or 550 °C. The lattice parameters of Li_6PS_5Cl in the samples annealed at 400−600 °C have similar values as shown in Figure 3b, comparable to previously reported values.[12] Increasing the annealing temperature to 550 °C leads to a clear decrease in the background of the XRD patterns (seen in Figure 1), indicating that the amorphous fraction decreases and the crystalline fraction increases. In addition, the linewidth of the reflections is the smallest at 550 °C. This indicates that the largest average crystallite size is obtained after annealing at this temperature (Figure 3b), assuming that all line broadening is due to size broadening. The minimal amounts of precursor phases and the amorphous fraction and the maximum average crystallite size in the sample annealed at 550 °C all indicate that the most crystalline phase pure material is obtained under these conditions.

In the Li_6PS_5Cl argyrodite, three types of Li-ion jump distances can be distinguished, all required to provide macroscopic diffusion. These are jumps between the paired 48h sites (the doublet jump), between the different 48*h* pairs, which interconnected form a cage of Li-ion diffusion around the 4c sites (the intra-cage jump). The third type of jump connects the cages and is therefore referred to as the inter-cage jump.[19] The distances for these three types of jumps, obtained from the Rietveld refinement, are shown in Figure 3c and the Cl distribution over the 4a and 4c sites is shown in Figure 3d. The data for the BMA-Li_6PS_5Cl argyrodite sample prepared by the conventional mechanical milling route have been included for comparison. The jump distances have been shown to depend on the lattice parameters, where Kraft et al.[18] demonstrated that going from I, Br, to Cl, leads to smaller differences in the three jump distances. This is a result of the decreasing lattice parameters as a function of decreasing halogen ion radius. For Li_6PS_5Cl the three jump distances were reported to differ at most by 0.7 Å.[18] Interestingly, the present results show a clear evolution in the Li^+−Li^+ jump distances as

DOI: 10.1021/acsami.8b07476
ACS Appl. Mater. Interfaces 2018, 10, 33296−33306

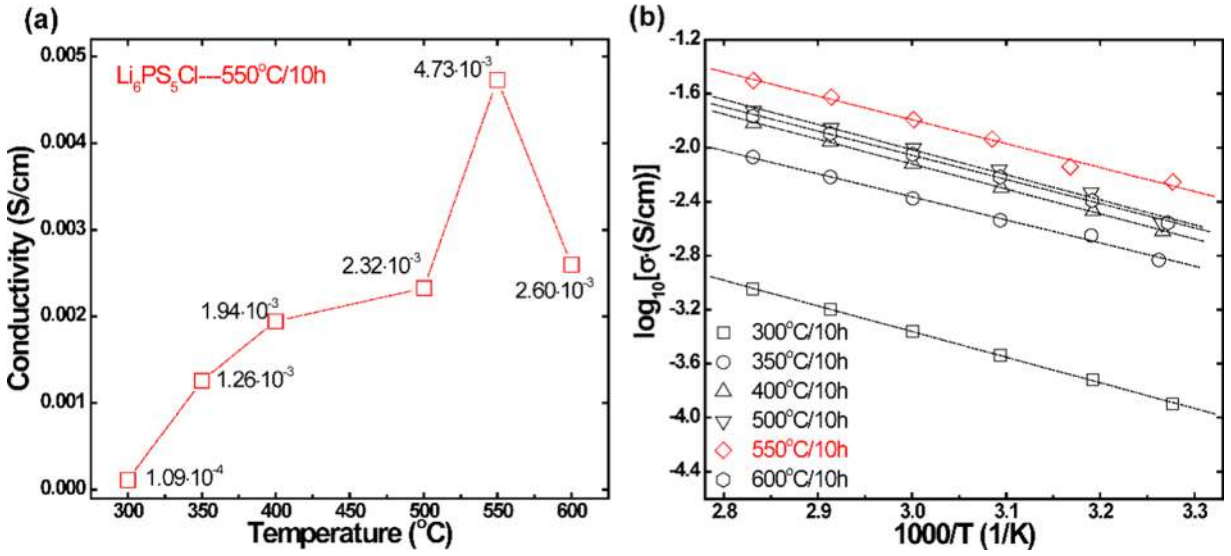

Figure 4. (a) Room temperature lithium ion conductivity of SSM-Li_6PS_5Cl annealed at different temperatures. (b) Arrhenius plots of SSM-Li_6PS_5Cl annealed at different temperatures.

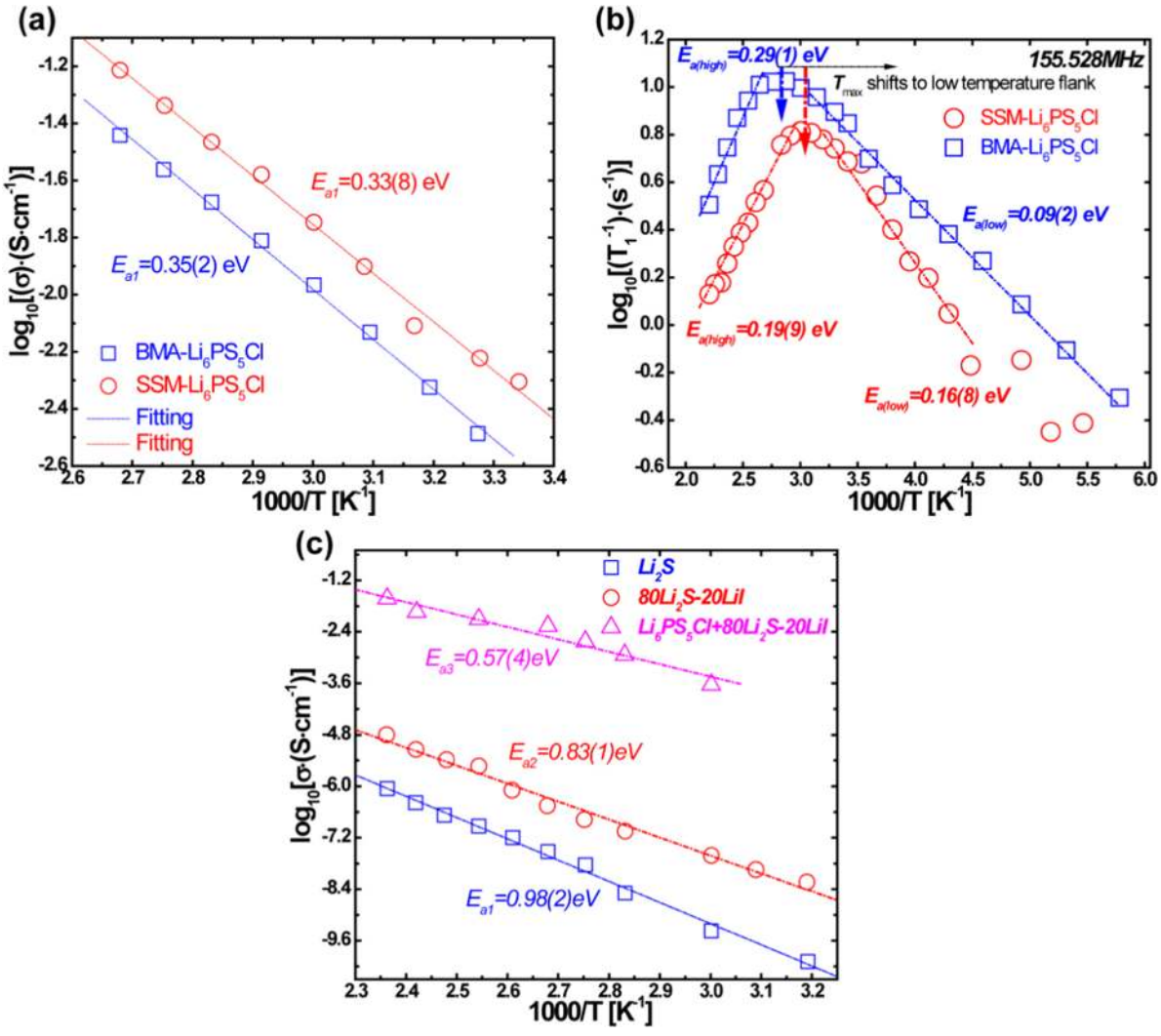

Figure 5. (a) Temperature dependence of the ionic conductivity for BMA-Li_6PS_5Cl and SSM-Li_6PS_5Cl. The impedance spectrum was measured from 30 to 100 °C. (b) ^7Li spin−lattice relaxation times of BMA-Li_6PS_5Cl and SSM-Li_6PS_5Cl. (c) Arrhenius plots of the ionic conductivity of pellets made from Li_2S, 80Li_2S−20LiI, and the mixture of Li_6PS_5Cl and 80Li_2S−20LiI. The ratio of the mixtures and the pressure used to make the pellet corresponds to that of the assembled solid-state battery.

DOI: 10.1021/acsami.8b07476
ACS Appl. Mater. Interfaces 2018, 10, 33296−33306

a function of annealing temperature, despite the similar lattice parameters as seen in Figure 3b,c. For the SSM-Li_6PS_5Cl annealed at 550 °C, the jump distances differ by values of not more than 0.1 Å, lower than the 0.7 Å reported by Kraft et al.[18] The Cl distribution over the 4a and 4c sites, the phase purity and crystallinity display significant variation as a function of annealing temperature, as shown in Figure 3. Rao et al.[14] showed that the Cl occupancy on the 4c sites increases to 50% for an annealing temperature of 400 °C, where the Cl and S mixing over the 4a and 4c sites is presumably a result of the similar S and Cl ionic radii (1.81 pm for Cl^- and 1.84 pm for S^{2-}). Increasing the annealing temperature to above 400 °C increases the Cl occupancy on the 4c site, indicating a slight preference for Cl to occupy this site.[14] At present, a similar trend is observed i.e., an increased Cl occupancy on the 4c site up to annealing temperatures of 500 °C. However, at an annealing temperature of 550 °C, the Cl occupancy on the 4c sites is slightly lower than for the sample annealed at 500 °C, and significantly higher for the sample annealed at 600 °C as seen in Figure 3d. It is worth noting that at 550 °C the total amount of Cl is closest to the target Li_6PS_5Cl composition. This most likely relates to the lowest fraction of precursor phases left at 550 °C and the highest crystallinity, as shown in Figure 3a,b, leading to the most phase-pure material closest to the target composition. It should be noted that the sample annealed at 500 °C also shows a higher lithium ion conductivity than samples annealed at lower temperatures, which is attributed to the lower amount of impurity phases in the sample as shown in Figure 3a and the larger average crystallite size depicted in Figure 3b.

To correlate the structural properties to the Li-ion conductivity, AC impedance measurements of SSM-Li_6PS_5Cl materials annealed at different temperatures were performed in a temperature range of 25−120 °C. The room temperature lithium ion conductivity as a function of annealing temperature is shown in Figure 4a and the temperature-dependent conductivities for the samples prepared at different annealing temperatures are shown in Figure 4b. The samples annealed at temperatures exceeding 300 °C displayed a much higher Li-ion conductivity. When the pristine mixture was annealed at 300 °C, precursor phases with a much lower lithium ion conductivity, such as Li_2S and LiCl were present in the annealed sample, impeding lithium ion conduction. The maximum value of the conductivity was found at 550 °C, which was also significantly higher than that determined for the BMA-Li_6PS_5Cl material as discussed below. The activation energies of the Li-ion conductivities of samples obtained after annealing at different temperatures, derived from temperature-dependent impedance spectroscopy and shown in Figure 4b, are 0.36 eV for 300 °C, 0.32 eV for 350 °C, 0.35 eV for 400 °C, 0.35 eV for 500 °C, 0.33 eV for 550 °C, and 0.34 eV for 600 °C, respectively. Rao et al.[14] showed that to reach a room temperature conductivity of 1 mS cm^{-1} and a low activation energy of 0.16 eV for Li_6PS_5Cl, the samples synthesized by mechanical milling followed by the annealing route had to be heat-treated to at least 250 °C. The present direct solid-state synthesis route by direct annealing at 550 °C, results in a higher lithium ion conductivity (4.96 mS cm^{-1} at 26.2 °C). However, one should be cautious while comparing impedance spectroscopy results as differences based on the pellet morphology and contacts of the electrodes with the pellet may be found.

For direct comparison between the annealing and mechanical milling preparation routes, impedance spectroscopy was performed from 30 to 100 °C for both the BMA-Li_6PS_5Cl and SSM-Li_6PS_5Cl annealed at 550 °C, the results of which are shown in Figure 5a and the spectra at selected temperatures are shown in Figure S2. At 32 °C, the conductivity of SSM-Li_6PS_5Cl is 5.99×10^{-3} S cm^{-1}, which is higher than the 3.25×10^{-3} S cm^{-1} obtained for BMA-Li_6PS_5Cl. Also, at 100 °C, the conductivity of SSM-Li_6PS_5Cl is higher at 0.061(1) S cm^{-1} compared to the 0.036(1) S cm^{-1} obtained for BMA-Li_6PS_5Cl. The temperature dependence of the conductivity for both BMA-Li_6PS_5Cl and SSM-Li_6PS_5Cl materials obeys an Arrhenius equation, $\sigma = A \exp(-E_a/RT)$. As displayed in Figure 5a, the activation energy for the conductivity deduced from the Arrhenius behavior is smaller for the SSM-Li_6PS_5Cl at 0.33(8) than 0.35(2) eV obtained for BMA-Li_6PS_5Cl, indicating more facile Li-ion diffusion in the former.

While the conductivity obtained from the impedance data potentially includes contributions from other charge carriers and from interfaces, solid-state ^{7}Li NMR selectively probes Li-ion motion on short diffusion length scales, reflecting the intrinsic Li-ion mobility.[24,25] To compare the intrinsic Li-ion mobility, temperature-dependent ^{7}Li spin−lattice relaxation rate $(1/T_1)$ measurements were performed for both BMA-Li_6PS_5Cl and SSM-Li_6PS_5Cl, the results of which are shown in Figure 5b. The temperature dependence of the ^{7}Li spin−lattice relaxation (SLR) rates in the laboratory frame can be used to quantify the Li-ion jump frequency and the corresponding energy barrier. This is based on the assumption that the variation in spin−lattice relaxation is only induced by Li-ion mobility in the Li-containing material.[26,27] The hopping frequency is given by $1/\tau$, where τ is the average residence time between the subsequent jumps. When the hopping frequency is in the order of the Larmor frequency (ω_o), $1/T_1$ reaches a maximum as a function of temperature, indicating the maximum transfer of energy toward the Li-ion nuclear spin. In the laboratory frame, an absolute lithium jump rate can be deduced from the maximum condition $\tau \cdot \omega_o \approx 1$ which is valid at the maximum relaxation rate.[28] From Figure 5b, it is observed that the maximum SLR rate is reached at 333 K for SSM-Li_6PS_5Cl and at 345 K for BMA-Li_6PS_5Cl. This corresponds to the same lithium jump frequency (9.80×10^8 s^{-1}) calculated based on the above-described maximum $1/T_1$ relaxation condition. SSM-Li_6PS_5Cl displays the same lithium jump frequency at a lower temperature when compared to BMA-Li_6PS_5Cl, indicating that the SSM route results in a faster intrinsic Li-ion mobility, at least in the low-temperature regime (<100 °C), consistent with the temperature-dependent impedance results. Assuming Arrhenius behavior for the Li-ion residence time, $\tau = \tau_o \exp(-E_a/(k_B T))$, the slope of the high and low-temperature regimes of the SLR rates are related to the activation energy for different Li-ion motional processes, yielding activation energies of 0.16 and 0.19 eV for SSM-Li_6PS_5Cl and 0.09 and 0.29 eV for BMA-Li_6PS_5Cl, for the local Li-ion (not contributing to macroscopic diffusion) and long-range (multiple jumps) Li-ion diffusion, respectively. The long-range activation energies of both BMA-Li_6PS_5Cl and SSM-Li_6PS_5Cl are smaller compared to that of the temperature-dependent impedance results. Most likely, this is because the activation energy deduced from the impedance includes both bulk and grain boundary contributions, while that obtained

DOI: 10.1021/acsami.8b07476
ACS Appl. Mater. Interfaces 2018, 10, 33296−33306

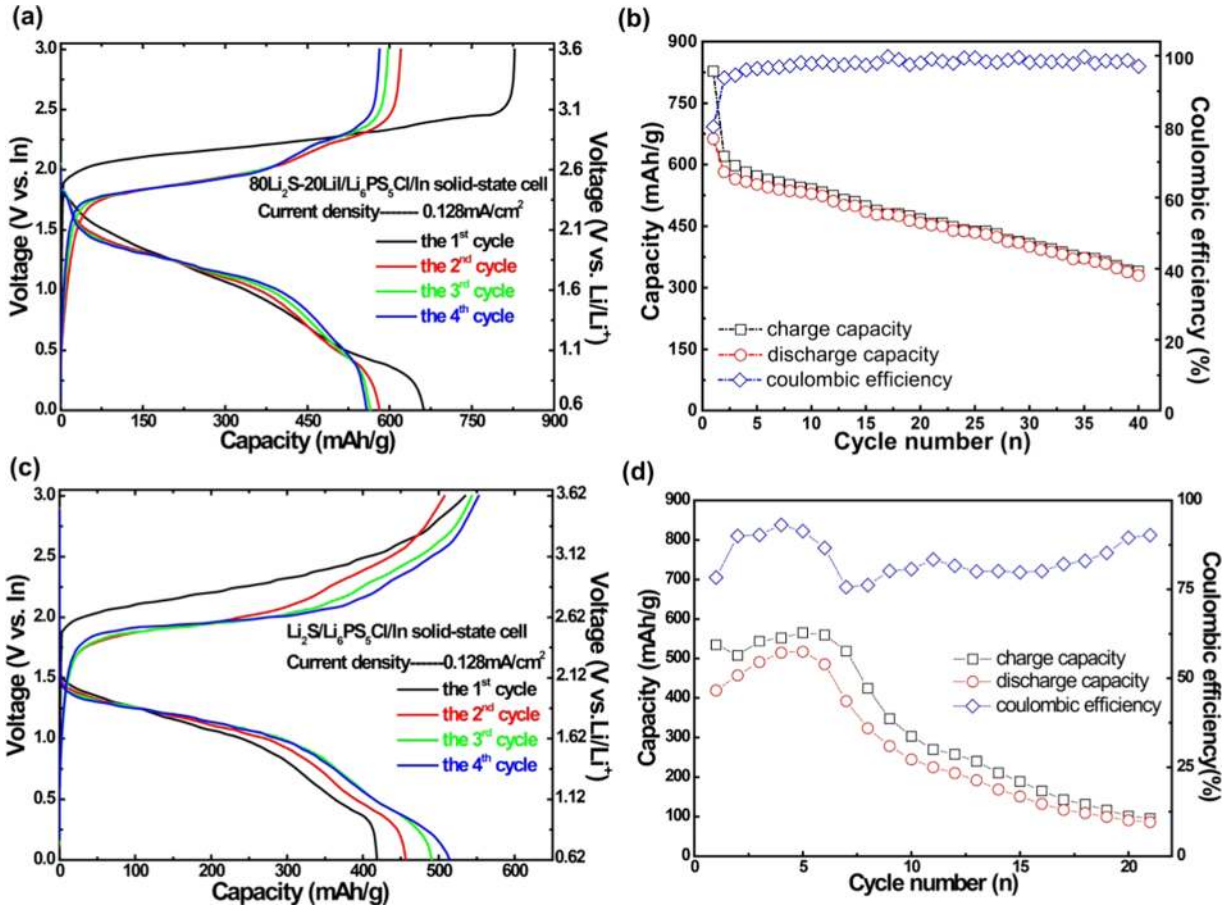

Figure 6. First four (dis)charge curves and the cycling performances of all-solid-state batteries $80Li_2S-20LiI/Li_6PS_5Cl/In$ (a, b) and $Li_2S/Li_6PS_5Cl/In$, based on the SSM-Li_6PS_5Cl material annealed at 550 °C, (c, d) measured at a current density of 0.128 mA cm^{-2} applied between 0 and 3.0 V vs In (0.62−3.62 V vs Li^+/Li).

with ^7Li SLR NMR reflects only the contribution from the bulk Li-ion mobility.

The structural analysis as shown in Figure 3 and previous research[14,15,18,19] on argyrodites indicates that many aspects play a role in determining the Li-ion conductivity. As demonstrated by Kraft et al.,[18] the smaller halogen radius going from I to Br to Cl decreases the lattice parameters, which results in a smaller inter-cage jump distance. This results in a decreased lattice softness, effectively promoting the ionic mobility, competing with the decreasing polarizability, going from I to Br to Cl, that has been generally associated with decreasing the ionic mobility.[18] Molecular dynamics simulations based on DFT of the argyrodite Li_6PS_5X (X = Cl, Br) structure demonstrated that detailed distribution of the halogen dopant over the 4a and 4c sites also has profound influence on the Li-ion mobility through the distribution of halogen charge compensating vacancies and jump frequencies.[19] The simulations suggest that the intra-cage jumps are promoted by Cl on the 4c sites, whereas the inter-cage diffusion is promoted by Cl on the 4a sites.[19] Because macroscopic diffusion requires both inter-cage and intra-cage diffusion, a homogeneous distribution of the halogen over the 4a and 4c sites is required for high Li-ion mobility.[14,19] Figure 3c indicates that the annealing temperature affects the Li^+-Li^+ jump distances, which cannot be explained by the nearly constant lattice parameters. However, the changing Cl distribution over the 4a and 4c positions as a function of annealing temperatures (see Figure 3d) suggests that this may also influence the Li^+-Li^+ jump distances. Indeed, when Cl replaces S on the 4c site, in the center of the Li-ion cage, the average Li-ion position is located further from the center of the cage,[19] most likely due to the smaller Coulombic attractive force. As a consequence, the Li cage becomes larger, which in combination with constant lattice parameters increases the doublet and intra-cage jump distances and reduces the inter-cage jump distance to similar values. Therefore, we suggest that the Cl distribution also influences the lattice softness, consequently influencing the jump frequencies, bringing together the mechanistic insights of Kraft et al.[18] and de Klerk et al.[19] The observation that the present material has very similar Li^+-Li^+ jump distances indicates that the preparation conditions result in the optimal S/Cl local environment for a high Li-ion mobility. For the overall conductivity, an additional factor is the structural homogeneity of the material. Not surprisingly, if the optimal local Cl environment for Li-mobility is more homogeneously achieved throughout the solid electrolyte material, this will result in more mobile Li-ions and hence in a higher overall conductivity. As previously reported, the mechanical milling preparation method for Li_6PS_5Br resulted in an inhomogeneous distribution over the 4a and 4c crystallographic sites, which was suggested to result in an inhomogeneous Li-ion mobility throughout the material.[15] At present the SSM-Li_6PS_5Cl material annealed at 550 °C shows the highest conductivity,

DOI: 10.1021/acsami.8b07476
ACS Appl. Mater. Interfaces 2018, 10, 33296−33306

and structurally it has the highest crystallinity at and the closest to target composition. This suggests that this material also has the largest degree of homogeneity. Therefore, we propose that Li^+-Li^+ jump distances that strongly determine the jump frequencies are determined by the Cl distribution over 4a and 4c sites. In addition, the homogeneous distribution of the dopant environments in the argyrodite structures is critical in achieving optimal Li-ion conductivity. At present, this is demonstrated by variation of the preparation conditions, at the same time providing the almost optimal preparation of the argyrodite Li_6PS_5Cl material.

To test the solid electrolyte material that displays the largest conductivity, the SSM-Li_6PS_5Cl annealed at 550 °C, solid-state batteries were prepared and electrochemically evaluated. Previous research[29] has shown that the ionic conductivity of the Li_2S cathode mixture can be improved by adding 20% (molar ratio) of LiI. This was shown to enhance the room temperature electrochemical performance of an all-solid-state cell prepared by combining an $80Li_2S-20LiI$ cathode with a $75Li_2S-25P_2S_5$ solid electrolyte.[29] In a similar manner, we prepared all-solid-state batteries by combining pristine nano-Li_2S and $80Li_2S-20LiI$ cathodes with the SSM-Li_6PS_5Cl (annealed at 550 °C) solid electrolyte. Figure 6 shows the first four (dis)charge curves and the cycling performance of these two all-solid-state batteries, i.e., $Li_2S/Li_6PS_5Cl/In$ and $80Li_2S-20LiI/Li_6PS_5Cl/In$. Both solid-state batteries were galvanostatically cycled with the same (dis)charge current density of 0.128 mA cm^{-2} between 0 and 3.0 V vs Indium to evaluate the electrochemical performance. The capacities are normalized to the mass of the nano-Li_2S and the $80Li_2S-20LiI$ active material. The initial charge and discharge capacities of $Li_2S/Li_6PS_5Cl/In$ solid-state cell are 534.7 and 418.7 mAh g^{-1}, yielding a Coulombic efficiency of 78.3%. For the $80Li_2S-20LiI/Li_6PS_5Cl/In$ all-solid-state battery, the corresponding initial charge and discharge capacity are 828.0 and 662.6 mAh g^{-1} and the initial Coulombic efficiency is 80.0%, significantly better than that of the $Li_2S/Li_6PS_5Cl/In$ solid-state cell. As shown in Figure 6d, after 21 cycles, the $Li_2S/Li_6PS_5Cl/In$ solid-state cell retains a capacity below 100.0 mAh g^{-1}. By introducing LiI in the $Li_2S-Li_6PS_5Cl$ cathode mixture, the cycling performance of the all-solid-state $80Li_2S-20LiI/Li_6PS_5Cl/In$ battery is significantly improved as shown in Figure 6b. As shown in Figure 6b,d, the changes in Coulombic efficiency for both all-solid-state batteries suggest that side reactions occur during the cycling of both cells, which may be associated with the decomposition of the solid electrolyte in both the cathode mixture and the solid electrolyte layer.[30] Previous research has reported that the decomposition of the solid electrolyte leads to the formation of products at the interface which can be expected to retard the Li^+ mobility and lead to a large interfacial charge transfer resistance during cycling.[30−32] XPS data has shown that Li_6PS_5Cl has an electrochemical redox activity in the positive electrode, which can be partially oxidized into LiCl, P_2S_5, and polysulfides Li_2S_n upon charge.[31] The introduction of LiI in the cathode mixture may work as a protective layer separating particles of the Li_2S active material and the solid electrolyte, reducing the redox reaction, potentially explaining the better cycling performance of the $80Li_2S-20LiI/Li_6PS_5Cl/In$ all-solid-state battery.

To evaluate the electrochemical stability of SSM-Li_6PS_5Cl (550 °C) against the lithium metal, a galvanostatic cycling test was performed. Lithium was plated and stripped in a $Li/Li_6PS_5Cl/Li$ symmetric cell at room temperature with a constant current density of 0.1 mA cm^{-2}, the result of which is shown in Figure S3. The voltage increases slowly upon cycling, indicating an unstable interface and an increased interfacial resistance between SSM-Li_6PS_5Cl and the Li-metal. Previous work has shown that Indium foil is a suitable anode material for the Li_6PS_5X (X = Cl, Br)-based all-solid-state battery.[15,21] Cyclic voltammograms of both Li_2S/SSM-Li_6PS_5Cl/In and $80Li_2S-20LiI$/SSM-Li_6PS_5Cl/In all-solid-state cells were investigated by applying different voltage windows from 0 to 3.0 to 4.28 V vs In, as shown in Figure S4. The intensity of the cathodic and anodic peaks can be attributed to the charge and discharge capacities, and the difference between these peaks is a rough indication of cycling efficiency. It can be observed from Figure S4 that the $80Li_2S-20LiI$/SSM-Li_6PS_5Cl/In all-solid-state cell displays a better cycling efficiency compared to the Li_2S/SSM-Li_6PS_5Cl/In cell, although cyclic voltammetry is not accurate in determining the detailed electrochemical stability. Moreover, compared to our previously reported results combining BMA-Li_6PS_5Cl and Li_2S in a cathodic mixture,[24] both Li_2S/SSM-Li_6PS_5Cl/In and $80Li_2S-20LiI$/SSM-Li_6PS_5Cl/In solid-state cells show larger initial discharge capacities with a higher initial cycle coulombic efficiency. It should be noted that the present capacities were attained by cycling at a higher (dis)charge current density i.e., 0.128 mA cm^{-2}, compared to the 0.064 mA cm^{-2} used previously. There are two possible reasons for the better electrochemical performance of the present solid-state cell. First, due to the improved room temperature Li-ion conductivity of SSM-Li_6PS_5Cl prepared by the present synthesis route, which is supported by both the temperature-dependent AC impedance and ^7Li spin−lattice relaxation NMR measurements described in the previous section. Second, introducing LiI will enhance the Li-ion conductivity of the cathode material,[29] as shown in Figure 5c. After the introduction of 20% (mol) of LiI, the lithium ion conductivity of the cathode is improved and its activation energy is decreased. Moreover, the rate capability of both Li_2S/SSM-Li_6PS_5Cl/In and $80Li_2S-20LiI$/SSM-Li_6PS_5Cl/In all-solid-state batteries under various charge/discharge current densities (0.25, 0.63, and 2.5 mA cm^{-2}) were performed and are shown in Figure S5. Although the rate performances of both all-solid-state batteries were poor, the latter showed higher discharge capacities than that of the former under various current densities, confirming that the electrochemical performance was improved by the introduction of LiI in the cathode mixture. To find the origin of this improvement, electrochemical impedance spectroscopy (EIS) before and after the rate capability measurements were performed to determine the change in resistance. EIS results in Figure S6 show that by introducing the LiI in the cathode mixture, both the resistances of the solid electrolyte and of the interfacial contact increases more slowly. However, the result reported here (Figure 6b,d) is not as good as that reported by Han et al.[33] They prepared a homogeneous $Li_2S-C-Li_6PS_5Cl$ nanocomposite electrode via a wet chemical method and achieved a large reversible capacity of 830 mAh g^{-1} at 0.18 mA cm^{-2} for 60 cycles. This gives us a hint that to improve the electrochemical performance of lithium argyrodite-based all-solid-state batteries fabrication of better interfacial contacts is essential.[34−36]

CONCLUSIONS

Argyrodite Li_6PS_5Cl with an ionic conductivity of up to 4.96×10^{-3} S cm^{-1} at 26.2 °C was synthesized by a simple direct

DOI: 10.1021/acsami.8b07476
ACS Appl. Mater. Interfaces 2018, 10, 33296−33306

solid-state method; avoiding the complexity of the conventional high-energy milling route. SSM-Li_6PS_5Cl prepared with this route results in a higher Li-ion mobility compared to BMA-Li_6PS_5Cl prepared by the traditional milling route, as demonstrated, both by temperature-dependent AC impedance and spin−lattice relaxation ^{7}Li NMR measurements. Annealing at 550 °C results in the most phase-pure and crystalline solid electrolyte material. The resulting material is suggested to have the most homogeneous Cl distribution and optimal local Cl structure, which is necessary to achieve the optimal Li-ion conductivity by maximizing the Li-ion mobility as well as the number of mobile Li-ions. Combined with an improved Li_2S cathode, $80Li_2S-20LiI$, and an In anode, the prepared Li_6PS_5Cl shows promising electrochemical performance, delivering an initial discharge capacity of 662.6 mAh g^{-1} under the current density of 0.128 mA cm^{-2} and retaining 330.0 mAh g^{-1} after 40 cycles. Although high ionic mobility in a solid electrolyte is a key factor for solid-state batteries, electrolyte degradation and contact loss are major challenges that need to be addressed to achieve stable cycling.

■ ASSOCIATED CONTENT

Supporting Information

The Supporting Information is available free of charge on the ACS Publications website at DOI: 10.1021/acsami.8b07476.

Crystallographic parameters obtained from the simultaneous Rietveld refinement of XRD and ND data have been given; transmission electron micrographs, electrochemical impedance spectra, galvanostatic cycling in a Li/SSM-Li_6PS_5Cl/Li symmetric cell, cyclic voltammograms at different voltage windows, and rate performance measurements have also been depicted (PDF)

■ AUTHOR INFORMATION

Corresponding Author

*E-mail: m.wagemaker@tudelft.nl.

ORCID

Long Zhang: 0000-0002-4861-1471

Marnix Wagemaker: 0000-0003-3851-1044

Notes

The authors declare no competing financial interest.

■ ACKNOWLEDGMENTS

The research leading to these results has received funding from the European Research Council under the European Union's Seventh Framework Program (FP/2007−2013)/ERC Grant Agreement no. [307161] of M.W. Support from the Dutch organization of scientific research (NWO) for the solid-state NMR facility for advanced materials science in Nijmegen is gratefully acknowledged. The solid-state NMR facility for advanced materials science at the Radboud University is greatly acknowledged for supporting this research. The assistance of Frans Ooms, Michel Steenvoorden, and Kees Goubitz is gratefully acknowledged.

■ REFERENCES

(1) Jung, Y. S.; Oh, D. Y.; Nam, Y. J.; et al. Issues and Challenges for Bulk-Type All-Solid-State Rechargeable Lithium Batteries Using Sulfide Solid Electrolytes. *Isr. J. Chem.* **2015**, *55*, 472−485.

(2) Cao, C.; Li, Z.-B.; Wang, X.-L.; et al. Recent Advances in Inorganic Solid Electrolytes for Lithium Batteries. *Front. Energy Res.* **2014**, *2*, No. 25.

(3) Tatsumisago, M.; Nagao, M.; Hayashi, A. Recent Development of Sulfide Solid Electrolytes and Interfacial Modification for All-Solid-State Rechargeable Lithium Batteries. *J. Asian Ceram. Soc.* **2013**, *1*, 17−25.

(4) Takada, K. Progress and Prospective of Solid-State Lithium Batteries. *Acta Mater.* **2013**, *61*, 759−770.

(5) Minami, T.; Hayashi, A.; Tatsumisago, M. Recent Progress of Glass and Glass-Ceramics as Solid Electrolytes for Lithium Secondary Batteries. *Solid State Ionics* **2006**, *177*, 2715−2720.

(6) Xie, D.; Chen, S.; Zhang, Z.; et al. High Ion Conductive Sb_2O_5-doped β-Li_3PS_4 with Excellent Stability against Li for All-Solid-State Lithium Batteries. *J. Power Sources* **2018**, *389*, 140−147.

(7) Tao, Y.; Chen, S.; Liu, D.; et al. Lithium Superionic Conducting Oxysulfide Solid Electrolyte with Excellent Stability against Lithium Metal for All-Solid-State Cells. *J. Electrochem. Soc.* **2016**, *163*, A96−A101.

(8) Janek, J.; Zeier, W. G. A Solid Future for Battery Development. *Nat. Energy* **2016**, *1*, No. 16141.

(9) Quartarone, E.; Mustarelli, P. Electrolytes for Solid-State Lithium Rechargeable Batteries: Recent Advances and Perspectives. *Chem. Soc. Rev.* **2011**, *40*, 2525−2540.

(10) Chen, S.; Xie, D.; Liu, G.; et al. Sulfide Solid Electrolytes for All-Solid-State Lithium Batteries: Structure, Conductivity, Stability and Application. *Energy Storage Mater.* **2018**, *14*, 58−74.

(11) Deiseroth, H. J.; Kong, S. T.; Eckert, H.; et al. Li_6PS_5X: A Class of Crystalline Li-Rich Solids With an Unusually High Li^+ Mobility. *Angew. Chem., Int. Ed.* **2008**, *47*, 755−758.

(12) Rayavarapu, P.; Sharma, N.; Peterson, V.; et al. Variation in Structure and Li^+-Ion Migration in Argyrodite-type Li_6PS_5X (X = Cl, Br, I) Solid Electrolytes. *J. Solid State Electrochem.* **2012**, *16*, 1807−1813.

(13) Boulineau, S.; Courty, M.; Tarascon, J.-M.; et al. Mechanochemical Synthesis of Li-Argyrodite Li_6PS_5X (X = Cl, Br, I) as Sulfur-Based Solid Electrolytes for All-Solid-State Batteries Application. *Solid State Ionics* **2012**, *221*, 1−5.

(14) Rao, R. P.; Sharma, N.; Peterson, V.; et al. Formation and Conductivity Studies of Lithium Argyrodite Solid Electrolytes using In-Situ Neutron Diffraction. *Solid State Ionics* **2013**, *230*, 72−76.

(15) Yu, C.; Ganapathy, S.; van Eck, E. R. H.; et al. Revealing the Relation between the Structure, Li-Ion Conductivity and Solid-State Battery Performance of the Argyrodite Li_6PS_5Br Solid Electrolyte. *J. Mater. Chem. A* **2017**, *5*, 21178−21188.

(16) Yubuchi, S.; Teragawa, S.; Aso, K.; et al. Preparation of High Lithium-Ion Conducting Li_6PS_5Cl Solid Electrolyte from Ethanol Solution for All-Solid-State Lithium Batteries. *J. Power Sources* **2015**, *293*, 941−945.

(17) Kim, D. H.; Oh, D. Y.; Park, K. H.; et al. Infiltration of Solution-Processable Solid Electrolytes into Conventional Li-Ion-Battery Electrodes for All-Solid-State Li-Ion Batteries. *Nano Lett.* **2017**, *17*, 3013−3020.

(18) Kraft, M. A.; Culver, S. P.; Calderon, M.; et al. Influence of Lattice Polarizability on the Ionic Conductivity in the Lithium Superionic Argyrodites Li_6PS_5X (X = Cl, Br, I). *J. Am. Chem. Soc.* **2017**, *139*, 10909−10918.

(19) de Klerk, N. J.; Rosłoń, I.; Wagemaker, M. Diffusion Mechanism of Li Argyrodite Solid Electrolytes for Li-Ion Batteries and Prediction of Optimized Halogen Doping: The Effect of Li Vacancies, Halogens, and Halogen Disorder. *Chem. Mater.* **2016**, *28*, 7955−7963.

(20) Bachman, J. C.; Muy, S.; Grimaud, A.; et al. Inorganic Solid-State Electrolytes for Lithium Batteries: Mechanisms and Properties Governing Ion Conduction. *Chem. Rev.* **2015**, *116*, 140−162.

(21) Yu, C.; van Eijck, L.; Ganapathy, S.; et al. Synthesis, Structure and Electrochemical Performance of the Argyrodite Li_6PS_5Cl Solid Electrolyte for Li-Ion Solid-State Batteries. *Electrochim. Acta* **2016**, *215*, 93−99.

(22) Larson, A. C.; Von Dreele, R. B. *GSAS: General Structure Analysis System*; Report LAUR 86-748; Los Alamos National Laboratory: Los Alamos, NM, 2004.

DOI: 10.1021/acsami.8b07476
ACS Appl. Mater. Interfaces 2018, 10, 33296−33306

(23) Toby, B. H.; Von Dreele, R. B. GSAS-II: the Genesis of A Modern Open-Source All Purpose Crystallography Software Package. *J. Appl. Crystallogr.* **2013**, *46*, 544−549.
(24) Yu, C.; Ganapathy, S.; de Klerk, N. J. J.; et al. Unravelling Li-Ion Transport from Picoseconds to Seconds: Bulk versus Interfaces in an Argyrodite Li_6PS_5Cl-Li_2S All-Solid-State Li-Ion Battery. *J. Am. Chem. Soc.* **2016**, *138*, 11192−11201.
(25) Gupta, A.; Murugan, R.; Paranthaman, M. P.; et al. Optimum Lithium-Ion Conductivity in Cubic $Li_{7-x}La_3Hf_{2-x}Ta_xO_{12}$. *J. Power Sources* **2012**, *209*, 184−188.
(26) Wilkening, M.; Heitjans, P. From Micro to Macro: Access to Long-Range Li^+ Diffusion Parameters in Solids via Microscopic $^{6,7}Li$ Spin-Alignment Echo NMR Spectroscopy. *ChemPhysChem* **2012**, *13*, 53−65.
(27) Kuhn, A.; Kunze, M.; Sreeraj, P.; et al. NMR Relaxometry as a Versatile Tool to Study Li Ion Dynamics in Potential Battery Materials. *Solid State Nucl. Magn. Reson.* **2012**, *42*, 2−8.
(28) Kuhn, A.; Choi, J.-Y.; Robben, L.; et al. Li Ion Dynamics in Al-doped Garnet-Type $Li_7La_3Zr_2O_{12}$ Crystallizing with Cubic Symmetry. *Z. Phys. Chem.* **2012**, *226*, 525−537.
(29) Takashi, H.; Akitoshi, H.; Masahiro, T. Li_2S-Based Solid Solutions as Positive Electrodes with Full Utilization and Superlong Cycle Life in All-Solid-State Li/S Batteries. *Adv. Sustainable Syst.* **2017**, *1*, No. 1700017.
(30) Zhang, W.; Leichtweiß, T.; Culver, S. P.; et al. The Detrimental Effects of Carbon Additives in $Li_{10}GeP_2S_{12}$-Based Solid-State Batteries. *ACS Appl. Mater. Interfaces* **2017**, *9*, 35888−35896.
(31) Auvergniot, J.; Cassel, A.; Foix, D.; et al. Redox Activity of Argyrodite Li_6PS_5Cl Electrolyte in All-Solid-State Li-Ion Battery: An XPS Study. *Solid State Ionics* **2017**, *300*, 78−85.
(32) Koerver, R.; Walther, F.; Aygün, I.; et al. Redox-Active Cathode Interphases in Solid-State Batteries. *J. Mater. Chem. A* **2017**, *5*, 22750−22760.
(33) Han, F.; Yue, J.; Fan, X.; et al. High-Performance All-Solid-State Lithium−Sulfur Battery Enabled by a Mixed-Conductive Li_2S Nanocomposite. *Nano Lett.* **2016**, *16*, 4521−4527.
(34) Yu, C.; Ganapathy, S.; Van Eck, E. R.; et al. Accessing the Bottleneck in All-Solid-State Batteries, Lithium-Ion Transport over the Solid-Electrolyte-Electrode Interface. *Nat. Commun.* **2017**, *8*, No. 1086.
(35) Luntz, A. C.; Voss, J.; Reuter, K. Interfacial Challenges in Solid-State Li Ion Batteries. *J. Phys. Chem. Lett.* **2015**, *6*, 4599−4604.
(36) Park, K. H.; Oh, D. Y.; Choi, Y. E.; et al. Solution-Processable Glass LiI-Li_4SnS_4 Superionic Conductors for All-Solid-State Li-Ion Batteries. *Adv. Mater.* **2016**, *28*, 1874−1883.

DOI: 10.1021/acsami.8b07476
ACS Appl. Mater. Interfaces 2018, 10, 33296−33306